Volume 1 | Number 1 | Jan 2013 | Pages 1–100

PCCP

Physical Chemistry Chemical Physics
www.rsc.org/pccp

ROYAL SOCIETY OF CHEMISTRY

This is an *Accepted Manuscript*, which has been through the Royal Society of Chemistry peer review process and has been accepted for publication.

Accepted Manuscripts are published online shortly after acceptance, before technical editing, formatting and proof reading. Using this free service, authors can make their results available to the community, in citable form, before we publish the edited article. We will replace this *Accepted Manuscript* with the edited and formatted *Advance Article* as soon as it is available.

You can find more information about *Accepted Manuscripts* in the **Information for Authors**.

Please note that technical editing may introduce minor changes to the text and/or graphics, which may alter content. The journal's standard **Terms & Conditions** and the **Ethical guidelines** still apply. In no event shall the Royal Society of Chemistry be held responsible for any errors or omissions in this *Accepted Manuscript* or any consequences arising from the use of any information it contains.

Journal Name

Physical Chemistry Chemical Physics

Dynamic Article Links ▶

ARTICLE TYPE

Failure mechanisms of nano silicon anodes upon cycling: an electrode porosity evolution model

Etienne Radvanyi,[a] Willy Porcher,[a] Eric De Vito,[a] Alexandre Montani,[a] Sylvain Franger[b]* and Séverine Jouanneau Si Larbi[a]*

With a specific capacity of 3600 mAh.g^{-1}, silicon is a promising anode active material for Li-ion Batteries (LIBs). However, because of the huge volume changes undergone by Si particles upon (de)alloying with lithium, Si electrodes suffer from a rapid capacity fading. A deep understanding of the associated failure mechanisms is necessary to improve these electrochemical performances. To reach this goal, we investigate here nano Si based electrodes by several techniques of characterization. Thanks to all these techniques, many aspects, such as the behaviour of the active material or the Solid Electrolyte Interphase (SEI) and the lithiation mechanisms are studied upon cycling. A clear picture of the failure mechanisms of nano Si based electrodes is provided. In particular, by combining Hg analyses, SEM observations of electrodes cross-sections, and EIS measurements, we follow the evolution of the porosity within the electrode. For the first time, our results clearly show a real dynamic of the pore size distribution: the first cycles lead to the formation of a micrometric porosity which is not present initially. During the following cycles, these large pores are progressively filled up with SEI products which form continuously at the Si particles surface. Thus, from the 50th cycle, Li$^+$ ions diffusion is dramatically hindered leading to a strongly heterogeneous lithiation of the electrode and a rapid capacity fading.

1. Introduction

The future development of all- or hybrid electric vehicles has put forward high-level requirements for Li-ion Batteries (LIBs). Thus, new electrode materials are needed to replace the commercial LiNi$_x$Mn$_y$Co$_z$O$_2$ or LiFePO$_4$ / graphite systems[1-3]. With a specific capacity of almost 3600 mAh.g^{-1} at room temperature, silicon is one of the most promising anode active materials[4-6]. However, because of the huge volume changes undergone by Si particles upon (de)alloying with lithium[7-9], Si electrodes suffer from a rapid capacity fading. These volume variations have been recognized to be responsible for at least: (i) a pulverization of the active material and a disintegration of the electrode[5,10] and (ii) a continuous formation of an unstable Solid Electrolyte Interphase (SEI) at the Si particles surface[11]. Many studies have been carried out to overcome these problems and indeed Si electrodes cyclability has been very much improved over the last 10 years at least when the electrodes are cycled *vs* Li metal. Thanks to the use of nanoparticles[10-18], which better sustain the mechanical strains, Si particles integrity can be maintained even when they are cycled at high capacities. In addition, it is well-known that the replacement of the polyvinylidene fluoride (PVDF) binder by carboxymethyl cellulose (CMC) favors a better bonding between Si and the conductive additive[19-22]; it greatly reduces the electrode

disintegration and the active material disconnection from the electronic network. Quite recently, the surface behaviour of Si electrodes and the associated SEI has emerged as another key issue[23-27]. In a similar electrolyte, the composition of the SEI which forms on silicon is very close to that which is found on graphite[23-27]. However, due to the considerable volume changes, the SEI is continuously reconstructed at the Si particles surface consuming irreversibly Li$^+$ and e$^-$ at each cycle. Besides, Si electrodes surface also concerns the Si oxides evolution upon cycling. Very complete studies from Philippe *et al*[24,27] show that the SiO$_2$ layer initially present at the particles surface, by reacting with the electrolyte and especially LiPF$_6$, can slowly transform into a SiO$_x$F$_y$ phase which deteriorates the interaction between the CMC binder and the Si particles. This phenomenon may degrade as well the electrochemical behaviour of the electrode. As we have just described, there is a lot of reasons for a Si electrode to fail and indeed, despite all the promising results obtained, cycling performances of Si electrodes remain so far unsatisfactory for a use in practical LIBs. In order to elaborate strategies to improve the coulombic efficiency and mitigate the rapid capacity drop, a clear picture of the failure mechanisms upon cycling is of major interest[4-6,28]. In the present work, we combine several techniques of characterization to study the aging of a nano Si based electrode. By using (i) conventional techniques: Scanning Electron Microscopy (SEM), X-ray Photoelectron Spectroscopy (XPS), Electrochemical Impedance

Spectroscopy (EIS), Focused Ion Beam (FIB) and (ii) unconventional techniques in the LIB research field: Auger Electron Spectroscopy (AES) and Hg porosimetry, we try to understand precisely the failure mechanisms of nano Si based electrodes. The evolution of the surface as well as the bulk of the electrode and the lithiation mechanisms upon cycling are analyzed and discussed. A special attention is dedicated to the evolution of the electrode porosity and its impact on the lithiation mechanisms.

2. Experimental section

2.1. Electrochemical testing

A Si based slurry made of an aqueous mixture of nano silicon (65 wt %, more information about the active material is provided in the SI, Figures S1 and S2), carbon fibers (25 wt %), and Carboxy Methyl Cellulose (CMC) (10 wt %, M_w = 250 kg. mol^{-1}, D.S. = 0.7) was coated on a 10 µm copper foil current collector. The loading of the electrode was ~1.5 mg of Si by cm². Electrodes were then cut into 14 mm diameter disk shape, dried 48 h and moved into an argon-filled glove box. CR2032 coin cells were assembled using a lithium metal foil as the counter electrode, a Celgard® 2400 separator, a Viledon® propylene foil wetted by a liquid electrolyte (1M $LiPF_6$ in ethylene carbonate (EC): diethyl carbonate (DEC) (wt % of 1:1)) and a working electrode. Galvanostatic charges and discharges were carried out with a current density of 0.3 mA.cm⁻² (corresponding to a C/20 rate based on a 3600 mAh.g^{-1} capacity) at 25°C using a battery tester (Arbin). After a complete discharge/charge cycle, the cells were cycled with a limited discharge capacity of 1200 mAh.g^{-1}. The cut-off potentials of charge and discharge were respectively 1.2 and 0.03 V *vs* Li^+/Li. After cycling, before further characterization (SEM, XPS, AES, Hg porosimetry, mass and thickness measurements), the cells were relaxed until the derivation of the potential was inferior to 1 mV.h^{-1}. Si electrodes were then removed from the coin cells in a glove box and washed twice with dimethyl carbonate (1 min per time).

2.2. SEM and FIB cross-sections

Electrodes were transferred from the glove box to the FIB/SEM Fast Entry Lock (FEL) room using a transfer vessel to avoid any exposure to air. The FIB/SEM equipment is a FIB ZEISS NVISION 55. Before achieving the cross-section of the electrode, a layer of 2 µm of tungsten was deposited at the surface of the sample. The FIB cut itself was then carried out by using 30 kV / 27 nA conditions for rough FIB cut and 30 kV / 700 pA for the final ionic polishing step.

2.3. XPS characterization

Electrodes were transferred directly from the glove box to the XPS FEL room using a sealed transfer vessel to avoid exposure to air. XPS measurements were carried out with a SSI spectrometer using a focused monochromatized Al Kα radiation (hν = 1486.6 eV). The pass energy was set to 25 eV allowing an energy resolution of approximately 670 meV. No charge neutralization was used. The binding energy scale was calibrated from the hydrocarbon C 1s at 285 eV.

2.4. AES characterization

The samples were transferred from the glove box to the AES FEL using again a sealed transfer vessel to avoid exposure to air. Auger measurements were achieved with a Physical Electronics 700Xi scanning Auger nanoprobe. The analyses were done at 5 kV / 5 nA. Spatial resolution as low as 20 nm can be reached while maintaining an energy resolution of 0.5%. AES depth profiles were obtained by using argon ion sputtering (1 keV / 1 µA) with a tilt of the samples of 30°. During sputtering, Zalar rotation with a speed of one rotation per min was systematically used. This technique improves sputtering homogeneity of the electrode surface. Auger data were analyzed by using Multipak software. AES intensities correspond to the peak-to-peak height of the derivative spectra.

2.5. Hg porosimetry measurements

Mercury intrusion and extrusion measurements were achieved by using a Micromeritics Autopore equipment. The pressure range was scanned from 0.01 to 200 MPa which roughly corresponds to a pore size from ~200 µm to ~5 nm. More information about these analyses is available in the SI (Figures S3-S8 and associated comments).

2.6. EIS measurements

A three-electrode pouch-cell was used for EIS investigations, the Si electrode being the working electrode and metallic lithium both counter and reference electrodes. Measurements were achieved by using a VMP3 Biologic system. The frequency range was scanned from 200 kHz to 10 mHz (with 10 frequencies scanned per decade) with a voltage sinusoidal perturbation amplitude of 10 mV (PEIS). The spectra were recorded at the end of charge/delithiation after relaxing the cell until the derivation of the potential was inferior to 1 mV.h^{-1}.

2.7. Mass and thickness measurements of the electrodes

After being washed in DMC, the Si electrodes were dried under vacuum for 1 h, weighed (± 0.01 mg) and their thickness measured by using a Palmer micrometer.

3. Results

3.1. Electrochemical performance

After a first complete electrochemical cycle whose impact is discussed in the Supporting Information (Figures S9 and S10 and corresponding comments), the Si electrodes were cycled with a lithiated capacity limited to 1200 mAh.g^{-1}. This capacity has been chosen following Kasavajjula *et al*'s calculations[6]: considering a cathode capacity of 200 mAh.g^{-1} and the 18650 standard format, the total capacity of a Li-ion cell is rather stable beyond an anode capacity of 1200 mAh.g^{-1}. Figure 1 shows the evolution of (A) the lithiation/delithiation capacities, (B) the coulombic efficiency, and (C) the lithiation voltage cut-off as a function of the cycle number. In addition, the voltage/capacity profiles are presented for cycles 2, 10, 50, and 80 (D). The results obtained here are very similar to others reported for Si electrodes in the literature[5,6,28]: (i) the capacity of 1200 mAh.g^{-1} can be maintained during less than 60 cycles and (ii) the average value of the coulombic efficiency from cycle 2 to cycle 100 is 0.981, far below 1. The lithiation voltage cut-off *vs* cycle number is more rarely shown: for our system, the cut-off potential is rather stable

(~0.2 V) during the first 40 cycles before a rapid decrease until reaching 0.03 V. This evolution is illustrated by the potential/capacity profiles: the results obtained for cycles 2 and 10 are almost identical with the presence of only one pseudo plateau at around 0.3 V for the lithiation process. Cycle 50 is characterized by: (i) a diminution of the capacity associated with this plateau (~800 mAh.g^{-1} *vs* almost 1200 mAh.g^{-1} for cycles 2

and 10) and (ii) the appearance of another pseudo plateau at 0.1 V indicated with the thick black arrow on Figure 1D. Both phenomena are observed and even accentuated for cycle 80: there is again a decrease of the capacity associated with the plateau at 0.3 V and an increase of the capacity related to the plateau at 0.1 V. In addition, the discharge voltage limit of 0.03 V is reached before lithiating a capacity equivalent to 1200 mAh.g^{-1}.
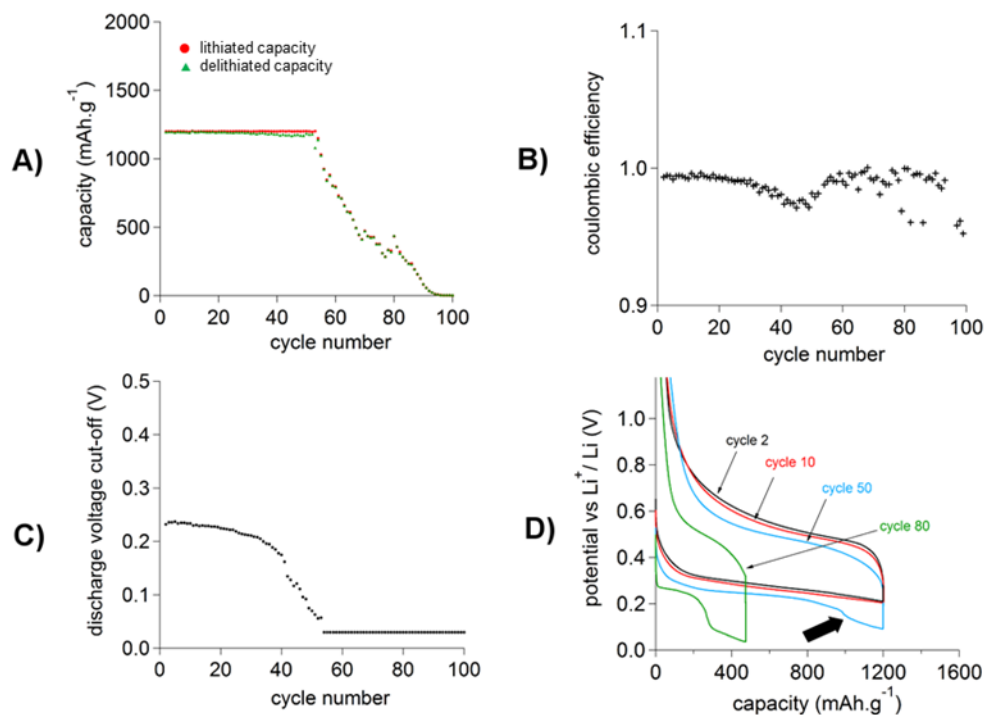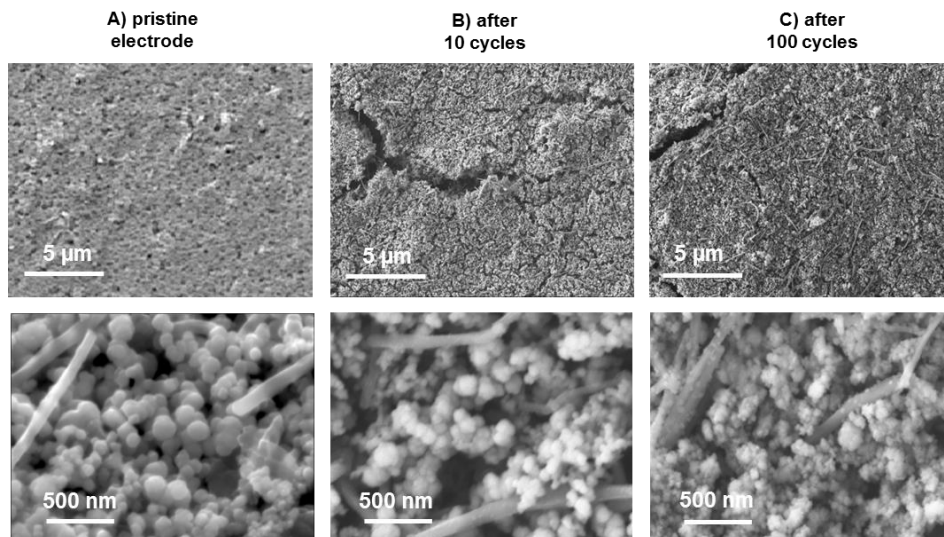

Fig. 1 A) Charge/delithiation and discharge/lithiation capacities *vs* cycle number. B) Coulombic efficiency *vs* cycle number. C) End of discharge/lithiation voltage *vs* cycle number. D) Potential/capacity profiles for cycles 2, 10, 50, and 80

3.2. Surface of the electrode

3.2.1. SEM characterization

Fig. 2 SEM images (5 µm and 500 nm scales) of the Si electrodes: A) pristine electrode, B) after 10 cycles, and C) after 100 cycles. For B) and C), the analyses were carried out at the end of charge/delithiation.

ARTICLE TYPE

Figure 2 shows the morphological changes undergone by the Si electrode surface upon cycling. According to the SEM images of the pristine electrode, initial Si particles are nanometric with a diameter close to 200 nm (500 nm image). The carbon fibers are 5 clearly visible as well; their average diameter is 150 nm. After 10 cycles, cracks appear at the electrode surface (5 μm image). The size of these cracks varies from few hundreds of nanometers to several micrometers. The appearance of fractures at the Si electrode surface is not surprising and has been reported 10 previously[23,29]. Concerning the Si particles, their morphological integrity may have been slightly affected by Li (des)insertion: after 10 cycles, the average diameter looks under 200 nm. For the carbon fibers, no change is visible. After 100 cycles, the cracks at the electrode surface are still present. Concerning the Si particles, 15 compared to cycle 10, their diameter has decreased again to reach ~100 nm. The integrity of the carbon fibers is maintained.
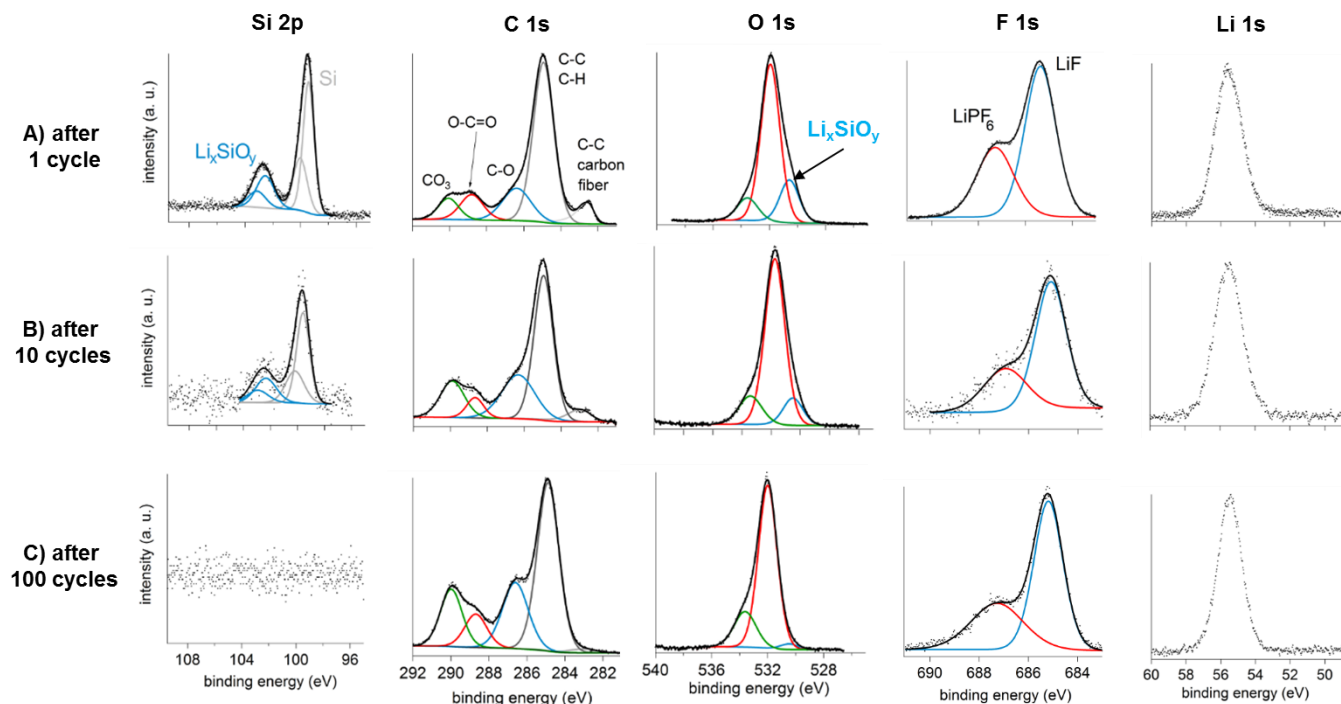
3.2.2.   XPS characterization

Figure 3 shows the XPS spectra obtained from the Si electrodes after 1, 10, and 100 cycles. The XPS analyses of the pristine 20 electrode as well as the P 2p spectra are available in the SI (Figures S11 and S12). After 1 cycle, C, O, F, P, and Li are detected. The presence of these elements can be directly related to the reduction of the electrolyte and the formation of the SEI at the electrode surface. The shapes of the spectra are in good 25 agreement with many XPS results carried out on Si electrodes by other groups[23-26,30-32]. C 1s spectrum shows 5 peaks. The first contribution at ~290 eV corresponds here to CO_3 and can be associated with the presence of carbonaceous species including Li_2CO_3 and/or lithium alkyl carbonates[33]. Both have actually 30 been widely reported as main components of the SEI which forms on graphite, tin or silicon when the electrode is cycled in an electrolyte made of $LiPF_6$ dissolved in carbonates[23,33,34]. The peaks at 288.5, 287, and 285 eV are attributed respectively to O-C=O, C-O, and C-C/C-H bonds. The detection of these 35 environments can firstly be explained by the presence of other species in the SEI such as oxalates and/or polyethylene oxide (-CH_2-CH_2-O-)$_n$ (POE), which have been previously found on negative electrodes[33,35,36]. As they are initially observed and attributed to the CMC (Figure S11), these peaks might also be 40 associated to the binder which is probably located, after 1 cycle, under the SEI but still detectable. In addition, the peak at 285 eV is of course partially related to hydrocarbon contamination.

Interestingly, another peak is observed on C 1s spectrum at a very low binding energy (~282.5 eV). This peak is attributed to the 45 carbon fibers. The energy gap standing between the carbon fibers and the other carbon compounds can be explained by a strong differential charging effect between the insulating SEI and the highly conductive additive[37]. The presence of carbonates and/or organic species such as PEO in the SEI is confirmed by the 50 detection of one major peak for O 1s at ~532 eV. F 1s shows two components which can correspond to (i) $LiPF_6$ salt (at ~687.5 eV in red) remaining at the electrode surface and (ii) LiF (at ~685.5 eV in blue) resulting from the reduction of the salt anion PF_6^-. One large peak is observed for Li 1s between 58 and 52 eV. Even 55 if it is very difficult to resolve it, these energies can be associated with species such as LiF, Li_2CO_3 or lithium alkyl carbonates. Si 2p shows two components. A first peak is found at 99.5 eV related to Si^0. As there is no contribution at lower energies, one can assume that there is no Li-Si phase remaining at the particles 60 surface at the end of the first charge[29]. Another peak is observed at 102.5 eV, attributed to a Li_xSiO_y phase in the literature[23,29,38,39]. In addition, the presence of Li_xSiO_y can explain the contribution at ~532.5 eV on O 1s spectrum. Interestingly, as our group already reported in a previous work[29], no SiO_2 is detected at the 65 particles surface. This layer, present before starting the electrochemical cycles (Figure S11), is completely reduced during the first electrochemical cycle. After 10 and 100 cycles, the general shape of C 1s, O 1s, F 1s, and Li 1s is similar to the one obtained after one cycle. Only small fluctuations are detected 70 suggesting that the SEI composition is rather stable upon cycling. However, a decrease of the signals associated with Si and the carbon fibers is observed: at the end of the 100th cycle, Si is not found and the peak corresponding to the carbon fibers on C 1s spectrum is very weak. This phenomenon can be related to an 75 increase of the SEI thickness. In addition, according to the Si spectrum obtained after 10 cycles, there is no evolution of the oxides present at the surface of the Si particles. Particularly, the formation of the damaging phase SiO_wF_z is not revealed upon cycling for our electrochemical system, probably because no SiO_2 80 remains at the particles surface after the first electrochemical cycle[23,27]. The interaction between the CMC binder and the active material can be maintained without using LiFSI as the Li salt[27].

Journal Name

Physical Chemistry Chemical Physics

Dynamic Article Links ▶

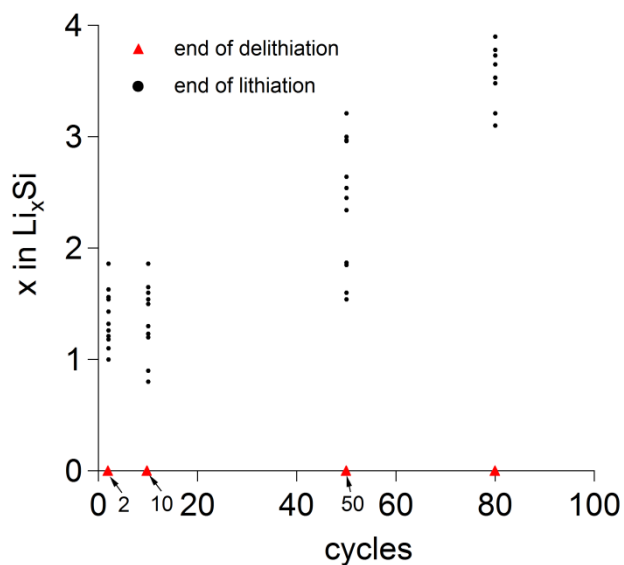**ARTICLE TYPE**

Fig. 3 XPS spectra (Si 2p, C 1s, O 1s, F 1s, and Li 1s core peaks) at the surface of the Si electrodes: A) pristine electrode, B) after 10 cycles, and C) after 100 cycles. The 3 electrodes were analyzed at the end of charge/delithiation.

3.2.3.   AES characterization

Fig. 4 Li-Si compositions obtained in several Si particles at the electrode surface by using AES. 8 electrodes were analyzed: after 2, 10, 50, and 80 cycles at the end of charge/delithiation and discharge/lithiation.

By using AES combined with Ar^+ sputtering, our group showed very recently the possibility of investigating individually Si nano particles and determining a Li concentration inside[29]. The experimental procedure and the conditions of analyses are detailed in previous studies[29,40]. AES is carried out here at the end of lithiation and delithiation of cycles 2, 10, 50, and 80. For each of the 8 electrodes, several Si particles (around 10) from the electrode surface are investigated. Based on the Li KLL and Si LVV signals obtained and by using the Alloy Reference Relative Sensitivity Factor (ARRSF) $R_{Li}^{Li_{15}Si_4}$, a composition of the Li-Si alloys found in the analyzed particles can be calculated. Inside all the investigated particles, once the SEI has been removed, the Li concentration obtained remains constant with sputter time, in good agreement with our previous results[29]. Figure 4 shows the Li_xSi compositions calculated from the AES analyses after 5 min of sputtering, which corresponds to a sputtered thickness of very approximately 50 nm. At the end of lithiation of cycles 2 and 10, the compositions of the Li_xSi alloys inside the Si particles at the surface of the electrode are very similar; in both cases, this composition varies from Li_1Si to Li_2Si. At the end of the 50th lithiation and after the same lithiated capacity of 1200 mAh.g^{-1}, the particles located at the surface of the electrode appear much more lithiated: the composition is found to be this time between $Li_{1.5}Si$ and Li_3Si. After 80 cycles, as the voltage cut-off limit of 0.03 V is quickly reached, the discharge capacity is only 435

mAh.g^{-1} (Figure 1). However, the Li concentration obtained in the particles is even higher: 3 to 4 Li per atom of Si. In addition to these results obtained after the lithiation of the electrodes, no Li alloyed with Si is found in the particles at the end of
5 charge/delithiation of all the cycles studied here.

3.3. Bulk of the electrode

3.3.1.   FIB cross-sections

To study the bulk of the electrode, FIB cut was used to observe cross-sections of the Si electrodes before any cycling, after 10
10 cycles, and after 100 cycles (Figure 5). In addition to the SEM analyses, Figure 5 shows black and white filtered images of the 1 µm SEM pictures. What is in white is supposed to correspond to the material located in the plan of the cross-section and what is in the depth appears in black. This division uses the different levels
15 of grey of the SEM image. As these levels are not easy to separate, the filtered images can contain some anomalies but still provide a local picture of the porosity inside the electrode.

As the copper current collector is visible on the 5 µm image of the pristine sample, the initial thickness of the Si electrode can be
20 determined: around 25 µm. From the 1 µm SEM image, the initial diameter of the Si particles which appear in very light grey on the image is found to be around 200 nm, in good agreement with the

SEM observations of the surface of the electrode (Figure 2A). The carbon fibers are also visible, in dark grey. According to the
25 filtered image, the initial porosity appears as quite homogeneous in terms of pore size and well distributed inside the electrode (following the same procedure, other areas of the electrode were analyzed and the results were very similar). After 10 cycles, some important changes are observed. The current collector is not seen
30 on the 5 µm SEM image indicating that the electrode thickness has increased and become greater than 25 µm. In addition, cracks, showed by red arrows on the 1 µm SEM and filtered images were formed upon cycling. Finally, a phenomenon of aggregation of Si nanoparticles is clearly showed here with the appearance of few
35 hundreds µm aggregates inside the electrode, surrounded by red circles on the 1 µm SEM and filtered images. After 100 cycles, the morphology of the cross-section has completely changed again. The electrode is made of micrometric aggregates which contain pores of few dozens of nm; these aggregates are separate
40 by very narrow channels. One of them is indicated by a red arrow on the 1 µm SEM and filtered images. In addition, higher resolution images which support these observations are provided in the SI (Figure S13).
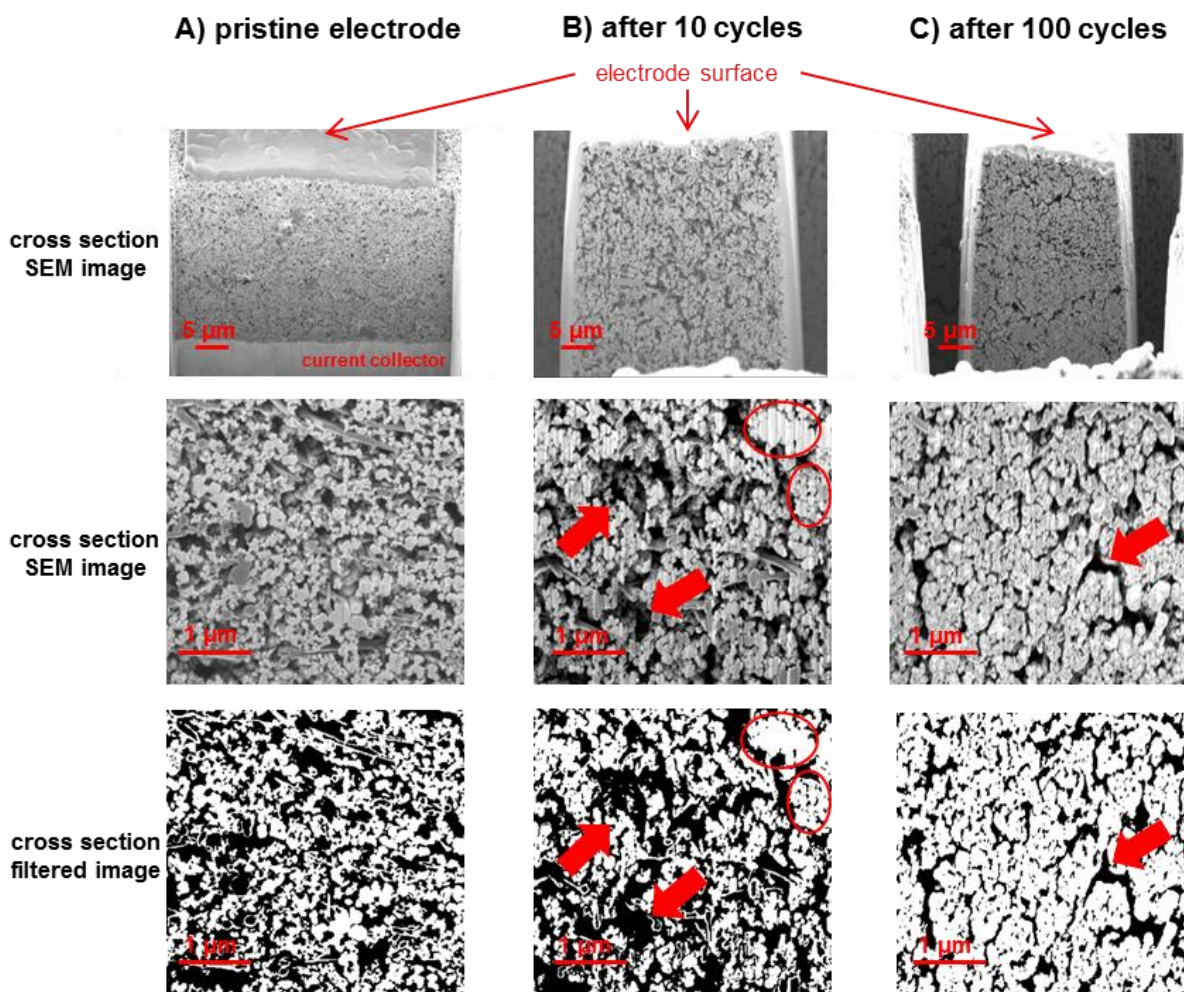
45   **Fig. 5** Cross-sectional SEM images (5 and 1 µm scales) of Si electrodes: A) pristine electrode, B) after 10 cycles, and C) after 100 cycles. In addition, black and white filtered images of the 1 µm scale images are presented. For B) and C), the observations were carried out at the end of charge/delithiation.
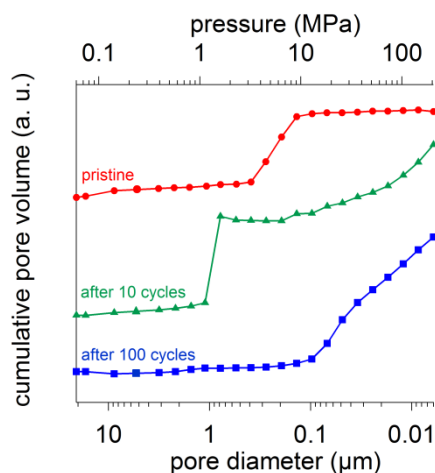
Journal Name

Physical Chemistry Chemical Physics

ARTICLE TYPE

3.3.2. Mercury intrusion porosimetry

Fig. 6 Mercury intrusion porosimetry analyses of Si electrodes for the
5   pristine, after 10 cycles, and after 100 cycles. For the cycled electrodes,
the analyses were carried out at the end of charge/delithiation.

To go further, mercury intrusion porosimetry was carried out on
these electrodes[41]. To calculate the correspondence between the
pressure and the pore size, pores are considered as cylinders with
10 a diameter D and Laplace's law is used:

$$D = \frac{-4\gamma cos\theta}{P}$$

γ is the interfacial tension of mercury taken here equal to 0.48
N.m^{-1} and θ the wetting angle generally considered as equal to
130°. At a pressure of P, pores with a diameter greater than D are
filled up with mercury, the others remain empty. We are aware
15 that considering the electrode pores as cylinders is a very strong
approximation (Figure 5). In addition, (i) the mass of the
analyzed samples is low, around few dozens of mg so it is
difficult to obtain accurate results, (ii) interpretation of mercury
intrusion / extrusion curves is often handled differently depending
20 on the authors, and (iii) the interaction between the mercury and
the electrode, notably with the SEI and especially at high pressure
is not known. However, we believe that these measurements
described below can provide interesting trends.

Figure 6 shows the intrusion curves obtained for 3 Si electrodes:
25 pristine, after 10 cycles, and after 100 cycles (supplemental data
and comments are available in ESI Figures S3-S8). The pristine
electrode exhibits a porosity characterized by a diameter which is
between 500 and 200 nm. The first 10 cycles deeply modify this
distribution: the initial diameter is no longer observed; instead, 2
30 distinct scales of porosity appear. The first one is a micrometric
porosity and the second one is associated with a pore diameter
lower than 100 nm. These results are in very good agreement
with the SEM images of the cross-section (Figure 5): the

micrometric porosity can be related to the formation of cracks
35 inside the electrode, whereas the much smaller pores can
correspond to the pores in or between the particles aggregates.
The porosimetry curve obtained after 100 cycles shows that the
micrometric porosity has completely disappeared. The only
porosity remaining after 100 cycles is characterized by a pore
40 diameter under 80 nm; again these measurements can be nicely
linked to the SEM observations obtained previously (Figure 5):
only porous aggregates and very narrow channels are visible on
the images. The cracks visible at the electrode surface (Figure
2C) are probably not present in the bulk of the electrode and
45 represent a very little mercury volume.

3.3.3. Summary

Table 1 Values of porosities calculated from FIB cut observations and Hg
intrusion analyses, mass and thickness obtained for 3 Si electrodes:
pristine, after 10 cycles, and after 100 cycles. For the cycled electrodes,
50 measurements were carried out at the end of charge/delithiation.

	Porosity from FIB	Porosity from Hg intrusion	Mass	Thickness
Pristine	43%	59%	M_i	25 µm
After 10 cycles	57%	74%	1.2 M_i	34 µm
After 100 cycles	29%	30%	3.1 M_i	58µm

a Footnote text.

From the observations of the cross-sections and the mercury
intrusion measurements, a porosity value can be estimated for
each electrode. The porosity from the SEM analyses is obtained
55 by using the cross-sectional filtered image. It is simply based on
the ratio between the black area and the total area of the image.
Concerning the porosity obtained from mercury intrusion, it uses
the total cumulative pore volume. Table 1 shows the values
calculated for the 3 electrodes analyzed in this section: pristine,
60 after 10 cycles, and after 100 cycles. In addition, the mass and
thickness of the electrodes have been measured and are actually
reported. The thickness is associated only with the electrode
without the current collector. The mass value is based on the
initial mass M_i of the pristine electrode. Upon cycling, both mass
65 and thickness increase. This phenomenon is not surprising and
has already been shown for Si electrodes[42]. Concerning the
porosity, we can first notice that the values obtained from the
cross-sections observation and mercury intrusion are quite
different. Both techniques contain some uncertainties, as
70 mentioned previously. However, the evolutions are similar in
both cases. Thus, during the first cycles, the porosity increases, in
good agreement with the values of mass and thickness: after 10
cycles, the mass is very close to the initial one whereas the
thickness of the electrode has increased. After 100 cycles,
75 according to both techniques, the porosity has dramatically
decreased and become even much lower than the porosity of the
pristine electrode.

3.4. Electrochemical Impedance Spectroscopy investigations

Every 10 cycles, an EIS measurement is carried out at the end of charge/delithiation. Figure 7 shows the results obtained after cycles 10, 50, and 100. The fitting data which are discussed later on are also presented. The first striking feature of the impedance evolution is the dramatic increase of the modulus: from 40 Ω after 10 cycles to 1000 Ω after 100 cycles, in good agreement with the degradation of the electrochemical performances of the Si electrode upon cycling (Figure 1). If we try to go further into the interpretation of the spectra, we should determine the frequencies associated with the different phenomena that can be observed by EIS. Two semi-circles are visible at High Frequencies (HF), *i. e.* f > 1 Hz. This HF region is typical of interfacial phenomena. By analyzing a Si electrode at several states of charge during one electrochemical cycle, we attributed the first semi-circle to the presence of the SEI (the surface film with an almost stable chemical composition[29] leads here to one semi-circle with a constant characteristic frequency $f_{SEI} \sim 50$ kHz) and the second semi-circle to the charge-transfer (CT) process; CT is coupled with a double layer (DL) capacitance which leads to one semi-circle, and the $R_{CT}C_{dl}$ product evolves with the operating voltage, *i. e.* with the lithium content for an alloying compound, so that the corresponding characteristic frequency, f_{CT}, evolves as well upon one electrochemical cycle.

We can note the decrease of the frequency associated with CT, almost 300 Hz after 10 cycles and only 60 Hz after 100 cycles, indicating that this electrochemical process becomes slower upon cycling. In addition to these two semi-circles, the impedance spectra systematically exhibit a more unusual curvature at Low Frequency (LF), ~0.5 Hz. In our case, the curvature is visible very early (after only 10 cycles). At that time, the Si electrode cycles relatively well; this behaviour is not compatible with a very slow interfacial phenomenon. Actually, this frequency domain is generally related to diffusion processes in the active material host lattice. As said previously, the Si material used in this study is nanometric with an average particle diameter close to 200 nm. Thus, it is hard to believe that the impedant phenomenon with this frequency of 0.5 Hz is associated with common semi-infinite Li diffusion in the active material (classical Warburg region with unidirectional Li diffusion, following the Fick's law). As suggested by Oumellal *et al*[28] and regarding our previous results obtained by SEM on electrodes cross-sections and by Hg porosimetry, we think that this curvature is more likely related to a hindered Li diffusion inside the porous electrode (limited matter transport). To take the latter into account, we have to model the porosity. Based on previous publications[43-53] and especially on de Levie's work[43], the equivalent circuit we finally obtain here to fit the LF region (see SI for details) is shown on Figure 8a). As the semi-circle associated with the CT and DL is not flattened at all (Figure 7), which means, in other terms, that the Constant Phase Element coefficient is very close to 1, we can consider that these interfacial phenomena (CT and DL) are not distributed within the porosity of the electrode but only occur at the outer surface of the electrode. Thus, in this model, the pores are electrochemically inactive and can simply be seen as electrolyte unidirectional tanks inducing a supplemental polarization. The pores are individually described by the association of R_p and C_p, In order to estimate, as easier as possible, the porous nature of the electrode, we made the approximation that the pores are identical in terms of volume and shape inside the electrode (no size distribution). N_p and R_p represent respectively the number of individual pores and the electrolyte resistance inside one pore. If more information about the fitting model is provided in SI, N_p can be seen here as the number of pores needed to model the porosity inside the electrode and R_p as the volume of one pore. The product N_p by R_p is thus related to the total "electrical equivalent" porosity of the electrode. Finally, the experiment data were fitted (Figure 7) by using the complete equivalent circuit presented on Figure 8b); Table 2 shows the electrical parameters obtained at the end of cycles 10, 30, 40, 50, 80, and 100.
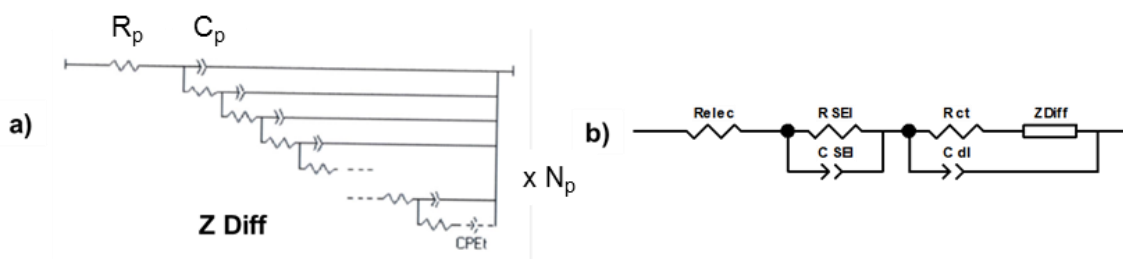
Journal Name

Physical Chemistry Chemical Physics

ARTICLE TYPE
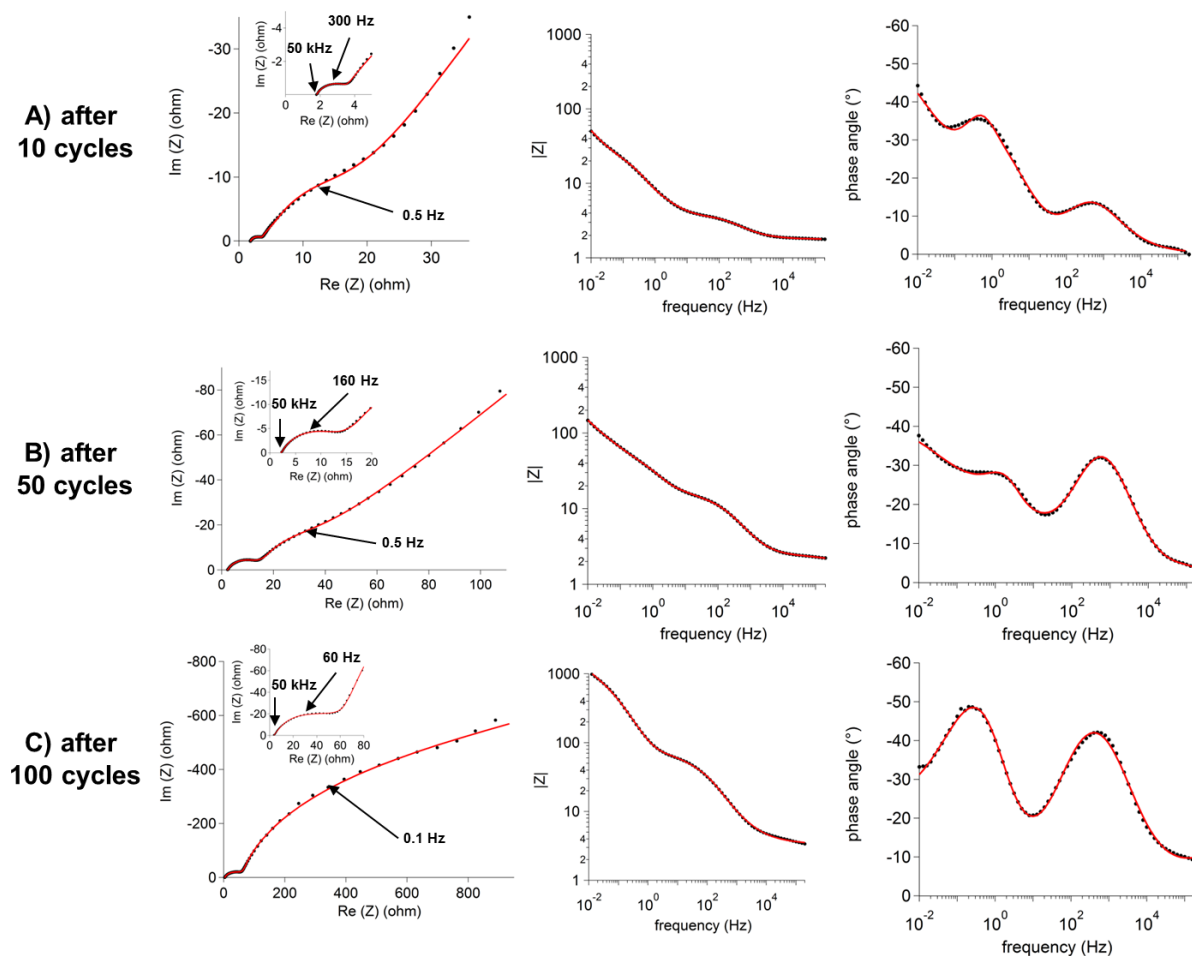
Fig. 7 Nyquist and Bode diagrams for the Si electrode A) after 10 cycles, B) after 50 cycles, and C) after 100 cycles. Both (●) experiment and (-) fitting data are presented.

5

Fig. 8 a) Model for the LF region and b) total equivalent circuit used to fit the experiment data.

Journal Name

Physical Chemistry Chemical Physics   Dynamic Article Links ►

ARTICLE TYPE

Table 2 Values obtained for the different parameters after fitting the experiment data with the equivalent circuit shown on Figure 8b). f_{SEI} and f_{CT} are the frequencies associated with respectively the SEI and the CT process. $|Z|_{LF}$ is the modulus of the impedance corresponding to a frequency range between 1 and 0.01 Hz.

	R_{elec} (Ω)	R_{SEI} (Ω)	f_{SEI} (kHz)	R_{CT} (Ω)	f_{CT} (Hz)	N_p	R_p (Ω)	N_p x R_p (Ω)	$|Z|_{LF}$ (Ω)
After 10 cycles	1.7	0.08	50	0.1	300	8	2.15	17.2	35
After 30 cycles	2	0.1	39	1.02	251	10	2.06	20.6	40
After 40 cycles	1.9	0.09	45	0.65	199	6	3.7	22.2	45
After 50 cycles	2.1	0.1	50	11.6	158	20	0.95	19	60
After 80 cycles	2	1.6	45	15.9	126	30	0.32	9.6	200
After 100 cycles	3.3	9.4	50	66.2	60	35	0.28	9.8	900

a Footnote text.

R_{elec} slightly increases upon cycling suggesting that the ionic conductivity of the electrolyte decreases. Concerning the results obtained for the SEI, they can be related to the XPS analyses (Figure 3). According to the XPS observations, the composition of the SEI is rather stable between the 10th and the 100th cycles, in good agreement with a stable corresponding characteristic frequency f_{SEI}. If R_{CT} noticeably increases upon cycling, the increase of the total impedance is mainly due to the augmentation of the low frequency impedance $|Z|_{LF}$ which corresponds to a frequency range between 1 and 0.01 Hz. As said previously, LF region is associated in our case with a constrained Li diffusion inside the electrode, which seems to be the main source of the electrode capacity fading upon cycling.

4. Discussion

4.1. The active material

According to the SEM images of the electrode surface (Figure 2), Li insertion/desinsertion has an impact on the active material morphology. The apparent diameter of the Si particles looks to decrease upon cycling from ~200 nm for the pristine electrode to ~100 nm after 100 cycles. This result was quite unexpected. Indeed, as the Si electrodes undergo a first complete electrochemical cycle, one can consider that afer cycle 2, the active material is amorphous silicon. According to McDowell *et al*[54], Si amorphous particles, up to a diameter of 870 nm, should not fracture or pulverize because of Li insertion/desinsertion. However, as reported by Gu *et al*[55] and our group previously[29], a kind of sintering phenomenon happens between neighboring particles during particles volume expansion. Upon delithiation, Si particles do not recover their initial morphology; Li desinsertion probably leads to the formation of smaller particles and aggregates as seen on Figure 5 at the end of delithiations 10 and 100. Based on Nuclear Magnetic Resonance analyses carried out elsewhere on similar electrodes[28], one can assume that no Li alloyed with Si is trapped inside these aggregates. However, this particles motion occurring upon Li (des)insertion strongly impacts the global morphology of the electrode.

4.2. The structure of the electrode and the lithiation mechanisms

During the first cycles, the thickness of the Si electrode increases. It comes with a complete transformation of the electrode porosity concerning (i) its value and (ii) the pore size distribution. If an undoubtedly quantitative value is hard to determine, an important increase of the porosity is obtained both by electrodes cross-sections observations and Hg porosimetry measurements (Table 1). In addition, Hg analyses show clearly upon cycling the appearance of two scales of porosity: a micrometric one and a sub-100 nm one. Because of this deeply heterogeneous porosity, Li^+ ions diffusion inside the electrode is hindered and is responsible for an impedant phenomenon. It is interesting to note that, in comparison to the figures obtained latter on, the values obtained after 10 cycles for the fitting parameters N_p and R_p, respectively 8 and 2.15 Ω, correspond to an electrolyte distributed inside the electrode in a few but large pores (Table 2). This anomalous Li^+ diffusion does not seem to impact the homogeneity of the lithiation through the electrode. According to the results obtained by AES at the end of lithiations 2 and 10 (Figure 4), the particles at the surface of the electrode are made of ~$Li_{1.5}Si$. This alloy corresponds to a Li concentration equal to approximately the third of $Li_{3.75}Si$, in good agreement with a lithiated capacity of 1200 mAh.g^{-1} distributed homogeneously inside the electrode. The electrochemical results concerning (i) the lithiation/delithiation curves (Figure 1) and (ii) the impedance measurements (Table 2) are rather stable during the 40 first cycles. In particular, the constant discharge voltage cut-off suggests that the composition of the Li-Si alloys found in the electrode at the end of the lithiation is stable until the 40th cycle. However, during these first 40 cycles, the low coulombic efficiency of ~99% indicates that some electrons are consumed irreversibly at each cycle. As said previously, it can be related to the permanent generation of SEI products at the Si particles surface during cycling. The XPS results indicate that the composition of this SEI is very close to that which forms on graphite; no deep evolution is observed upon cycling. In particular, some of the SEI products such as LiF and Li_2CO_3 contain lithium. Li^+ ions consumption causes a decrease of Li^+ concentration in the electrolyte that can explain a slight decrease of its ionic conductivity and the increase of the associated R_{elec} upon cycling (Table 2). Besides, R_{SEI} is very stable during the first 50 cycles. This evolution indicates that the thickness of the

SEI at the particles surface is rather constant at least until the 50th cycle, in good agreement with XPS analyses carried out elsewhere[23]. Thus, one can assume that some of the SEI products do not remain fixed to the particles but move and accumulate

5 inside the pores of the electrode, some of which are micrometric, as mentioned previously. This phenomenon has not a strong impact on the impedance of the system during the first 40 cycles. However, after 50 cycles, $|Z|_{LF}$ increases dramatically indicating that Li diffusion starts to be strongly impacted. In parallel,

10 electrode lithiation mechanisms are affected. The composition of the Li-Si alloys found by AES for the particles located at the surface of the electrode at the end of lithiation 50 has moved to $\sim Li_{2.5}Si$. As there is no Li alloyed with Si detected at the end of the delithiation, this high Li concentration cannot be related to Li

15 trapped in these particles during previous cycles. In addition, the presence of these Li-rich alloys is in good agreement with the decrease of the discharge cut-off potential shown on Figure 1. As the lithiated capacity is still equal to 1200 mAh.g^{-1} at the 50th cycle, these results indicate that lithiation is now heterogeneous.

20 If the particles located at the surface are more lithiated, one can assume that the active material in the bulk of the electrode, where Li^+ ions diffusion is the most hindered because of the pore filling, contains less lithium. With further cycling, the last described phenomena are exacerbated: (i) huge increase of $|Z|_{LF}$ (Table 2),

25 (ii) rapid decrease of the discharge voltage cut-off potential until reaching 0.03 V (Figure 1), and (iii) augmentation of the Li content in the particles from the surface of the electrode at the end of lithiation (Figure 4). Besides, the full lithiation/delithiation of the particles located at the electrode surface, the furthest from

30 the current collector, confirm that the capacity fading of nano Si based electrode comes from an ionic and not an electronic limitation. At the 100th cycle, no lithium can be inserted into the electrode. The porosity has considerably decreased compared to that of the first cycles (Table 1). Moreover, Hg analyses indicate

35 that the micrometric porosity, certainly completely filled up by SEI products, has disappeared; only pores under 80 nm are still observed. Interestingly, the values obtained for N_p and R_p, respectively 35 and 0.28 Ω (Table 2) can be associated with an electrolyte distributed in many but small pores, in very good

40 agreement with these last results. In addition, after 100 cycles, the product N_p by R_p has considerably diminished compared to cycle 10. This result is related to a decrease of the global electrode porosity supporting our model to fit the impedance spectra. Moreover, our results, detailed in the SI section, allow estimating

45 Li^+ diffusion coefficient, D_{Li+}. After 10 cycles, considering a pore diameter equal to 1 µm (Figure 6), D_{Li+} is equal to $\sim 10^{-10}$ cm².s^{-1}. This value is 10^4 inferior to the one obtained for the "fresh" electrolyte used here (ρ = 93.5 Ω.cm at 25 °C[56] and $D_{Li+} \sim 2.10^{-6}$ cm².s^{-1}[57]) and explains that the diffusion of Li^+ ions is clearly

50 visible on the impedance spectra. After 100 cycles, considering that the pore mean diameter is now 50 nm (Figure 6) and that the electrolyte resistivity is the same than that of a solid SEI (ρ = 10^7 Ω.cm, calculated by using R_{SEI} from Table 2 and the well-known equation: $R_{SEI} = 1/\sigma.d/S$), we obtain D_{Li+} inferior to 10^{-16} cm².s^{-1}.

55 This last value, a hundred times inferior to the Li^+ diffusion coefficient inside LiFePO$_4$[58] explains the very low capacity observed for our Si electrodes after 100 cycles.

Conclusions

By combining several techniques of characterization, the failure
60 mechanisms of nano Si based electrodes have been studied. Figure 9 summarizes the results obtained in this work. The first cycles lead to the formation of a micrometric porosity which is not present initially. During the following cycles, the SEI does not totally remain at the particles surface but partly accumulates
65 inside these large pores. Despite this early phenomenon, the lithiation is first homogeneous within the electrode. However, from the 50th cycle, the ionic percolation is no more maintained due to pore filling. During the lithiation process, some of the Si particles, more likely located at the surface of the electrode, are
70 more lithiated, whereas less Li inserts in the particles in the bulk of the electrode. With further cycling, the electrode becomes completely blocked from an ionic point of view: a rapid capacity fading is observed. The importance of the initial porosity for Si electrodes has already been reported in the literature[20,59,60].
75 However, the present study emphasizes the dynamic of the porosity upon cycling which is probably related to the mechanical motion undergone by the active material because of Li insertion/desinsertion. This "new" porosity has certainly a very strong impact on the SEI behaviour[61]. Consequently, in addition
80 to the efforts carried out to stabilize the SEI, we think that the parameters governing the particles dynamics such as carbon surface coating or the nature of the binder should be deeper considered. In addition, the interest of coupling AES, which allows investigating Li distribution inside the electrode, with
85 other interfacial investigating techniques, such as XPS and EIS, is here clearly demonstrated.
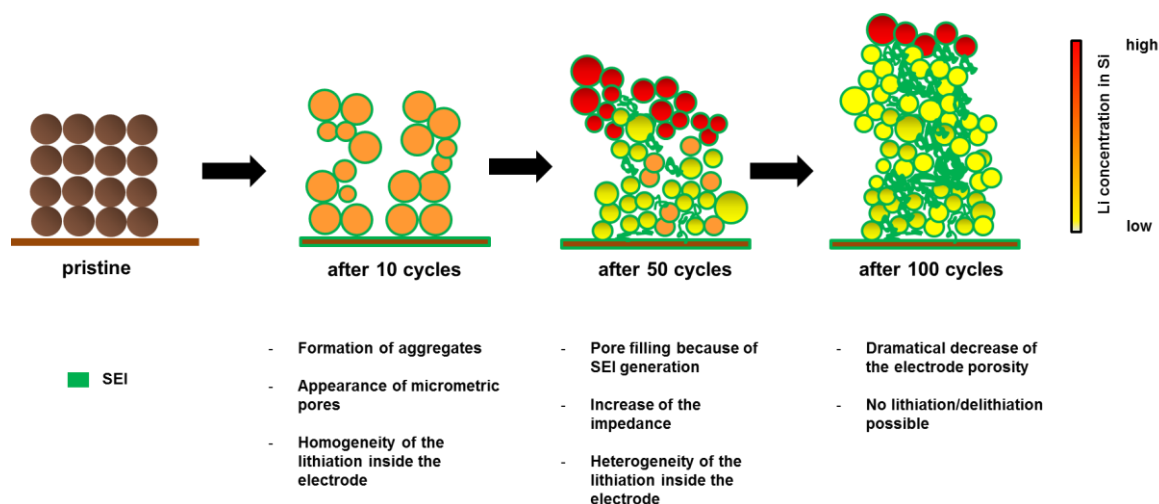
ARTICLE TYPE

Fig. 9 Schematic view of the failure mechanisms of nano Si based electrodes upon cycling.

Notes and references

5 *a French Commissary of Atomic and Alternative Energies (CEA), Laboratory of Innovation for New Energy Technologies and Nanomaterials (LITEN), 17 rue des martyrs, 38054 Grenoble, France. Fax: +33 438 784 383 ; Tel: +33 438 784 034; E-mail: severine.jouanneau@cea.fr*

10 *b ICMMO-ERIEE (UMR 8182), Université Paris Sud, 15 avenue Georges Clémenceau, 91045 Orsay, France. Tel: +33 169 156 312; E-mail: sylvain.franger@u-psud.fr*

† Electronic Supplementary Information (ESI) available: Figures S1-S13 corresponding to supplemental analyses and comments. See 15 DOI: 10.1039/b000000x/
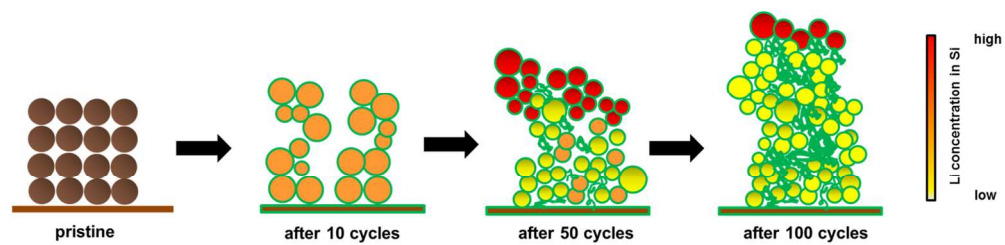
Acknowlegments

References

25
1 J. B. Goodenough and K. S. Park, *J. Am. Chem. Soc.*, 2013, **135**, 1167-1176.
2 B. Ellis, K. T. Lee and L. F. Nazar, *Chem. Mater.*, 2010, **22**, 691- 714.
30 3 V. Etacheri, R. Marom, R. Elazari, G. Salitra and D. Aurbach, *Energy Environ. Sci.*, 2011, **4**, 3243-3262.
4 D. Larcher, S. Beattie, M. Morcrette, K. Edström, J.-C. Jumas and J.-M. Tarascon, *J. Mater. Chem.*, 2007, **17**, 3759-3772.

5 W.-J. Zhang, *J. Power Sources*, 2011, **196**, 13-24.
35 6 U. Kasavajjula, C. Wang and A. J. Appleby, *J. Power Sources*, 2007, **163**, 1003-1039.
7 M. N. Obrovac and L. Christensen, *Electrochem. Solid-State Lett.*, 2004, **7**, A93-A96.
8 L. Y. Beaulieu, T. D. Hatchard, A. Bonakdarpour, M. D. 40 Fleischauer and J. R. Dahn, *J. Electrochem. Soc.*, 2003, **150**, A1457-A1464.
9 M. K. Y. Chan, C. Wolverton and J. P. Greeley, *J. Am. Chem. Soc.*, 2012, **134**, 14362-14374.
10 X.-H. Liu, L. Zhong, S. Huang, S. X. Mao, T. Zhu and J. Y. 45 Huang, *ACS Nano*, 2012, **6**, 1522-1531.
11 J. R. Szczech and S. Jin, *Energy Environ. Sci.*, 2011, **4**, 56-72.
12 H. Wu and Y. Cui, *Nano Today*, 2012, **7**, 414-429.
13 C. K. Chan, H. Peng, G. Liu, K. McIlwrath, X. F. Zhang, R. A. Huggins and Y. Cui, *Nat. Nanotechnol.*, 2008, **3**, 31-35.
50 14 L. Ji, Z. Lin, M. Alcoutlabi and X. Zhang, *Energy Environ. Sci.*, 2011, **4**, 2682-2699.
15 L. Ji and X. Zhang, *Electrochem. Comm.*, 2009, **11**, 1146-1149.
16 L. Ji and X. Zhang, *Carbon*, 2009, **47**, 3219-3226.
55 17 L. Ji and X. Zhang, *Energy Environ. Sci.*, 2010, **3**, 124-129.
18 M. R. Zamfir, H. T. Nguyen, E. Moyen, Y. H. Lee and D. Pribat, *J. Mater. Chem. A*, 2013, **1**, 9566-9586.
19 J. Li, R. B. Lewis and J. R. Dahn, *Electrochem. Solid-State Lett.*, 2007, **10**, A17-A20.
60 20 J.-S. Bridel, T. Azaïs, M. Morcrette, J.-M. Tarascon and D. Larcher, *Chem. Mater.*, 2010, **22**, 1229-1241.
21 B. Lestriez, S. Bahri, I. Sandu, L. Roué and D. Guyomard, *Electrochem. Comm.*, 2007, **9**, 2801-2805.
22 N. S. Hochgatterer, M. R. Schweiger, S. Koller, P. R. 65 Raimann, T. Wöhrle, C. Wurm and M. Winter, *Electrochem. Solid-State Lett.*, 2008, **11**, A76-A80.
23 B. Philippe, R. Dedryvère, M. Gorgoi, H. Rensmo, D. Gonbeau and K. Edström, *Chem. Mater.*, 2013, **25**, 394-404.
24 B. Philippe, R. Dedryvère, J. Allouche, F. Lindgren, M. 70 Gorgoi, H. Rensmo, D. Gonbeau and K. Edström, *Chem. Mater.*, 2012, **24**, 1107-1115.

Physical Chemistry Chemical Physics Accepted Manuscript

25   C. K. Chan, R. Ruffo, S. S. Hong and Y. Cui, *J. Power Sources*, 2009, **189**, 1132-1140.

26   C. Pereira-Nabais, J. Swiatowska, A. Chagnes, A. Gohier, S. Zanna, A. Seyeux, P. Tran-Van, C.-S. Cojocaru, M. Cassir and P. Marcus, *J. Phys. Chem. C*, 2014, **118**, 2919-2928.

27   B. Philippe, R. Dedryvère, M. Gorgoi, H. Rensmo, D. Gonbeau and K. Edström, *J. Am. Chem. Soc.*, 2013, **135**, 9829-9842.

28   Y. Oumellal, N. Delpuech, D. Mazouzi, N. Dupré, J. Gaubicher, P. Moreau, P. Soudan, B. Lestriez and D. Guyomard, *J. Mater. Chem.*, 2011, **21**, 6201-6208.

29   E. Radvanyi, E. De Vito, W. Porcher and S. Jouanneau Si Larbi, *J. Anal. At. Spectrom.*, 2014, **29**, 1120-1131.

30   V. Etacheri, Y. Haik, Y. Goffer, G. A. Roberts, I. C. Stephan, R. Fasching and D. Aurbach, *Langmuir*, 2012, **28**, 965-976.

31   M. Nie, D. P. Abraham, Y. Chen, A. Bose and B. L. Lucht, *J. Phys. Chem. C*, 2013, **117**, 13403-13412.

32   K. W. Schroder, H. Celio, L. J. Webb and K. J. Stevenson, *J. Phys. Chem. C*, 2012, **116**, 19737-19747.

33   P. B. Balbuena and Y. Wang, *Lithium-Ion Batteries: Solid-Electrolyte Interphase*, Eds, Imperial College Press: London, U.K., 2004.

34   H. Bryngelsson, M. Stjerndahl, T. Gustafsson and K. Edström, *J. Power Sources*, 2007, **174**, 970-975.

35   P. Verma, P. Maire and P. Novák, *Electrochim. Acta*, 2010, **55**, 6332-6341.

36   R. Dedryvère, S. Laruelle, S. Grugeon, L. Gireaud, J.-M Tarascon and D. Gonbeau, *J. Electrochem. Soc.*, 2005, **152**, A689-A696.

37   D. Briggs and J. T. Grant, *Surface Analysis by Auger and X-Ray Photoelectron Spectroscopy*, IM Publications, 2004.

38   B. Guo, J. Shu, Z. Wang, H. Yang, L. Shi, Y. Liu and L. Chen, *Electrochem. Comm.*, 2008, **10**, 1876-1878.

39   Q. Sun, B. Zhang and Z.-W. Fu, *App. Surf. Science*, 2008, **254**, 3774-3779.

40   E. Radvanyi, E. De Vito, W. Porcher, J. Danet, P. Desbois, J.-F. Colin and S. Jouanneau Si Larbi, *J. Mater. Chem. A*, 2013, **1**, 4956-4965.

41   C. Leon y Leon, *Adv. Colloid Interface Sci.*, 1998, **76-77**, 341-372.

42   D. Mazouzi, N. Delpuech, Y. Oumellal, M. Gauthier, M. Cerbelaud, J. Gaubicher, N. Dupré, P. Moreau, D. Guyomard, L. Roué and B. Lestriez, *J. Power Sources*, 2012, **220**, 180-184.

43   R. de Levie, *Advances in Electrochemistry and Electrochemical Engineering*, Wiley Interscience Ed: New York, 1967.

44   H. Keiser, K. D. Beccu and M. A. Gutjahr, *Electrochim. Acta*, 1976, **24**, 539-543.

45   M. Keddam, C. Rakotomavo and H. Takenouti, *J. Appl. Electrochem.*, 1984, **14**, 437-448.

46   M. Lefebvre, R. Martin and P. Pickup, *Electrochem. Solid-State Lett.*, 1999, **2**, 259-261.

47   J. Bisquert, G. Garcia-Belmonte, F. Fabregat-Santiago and A. Compte, *Electrochem. Comm.*, 1999, **1**, 429-435.

48   H. Song, Y. Jung, K. Lee and L. Dao, *Electrochim. Acta*, 1999, **44**, 3513-3519.

49   J. Bisquert, *Phys. Chem. Chem. Phys.*, 2000, **2**, 4185-4192.

50   D. Qu, *J. Power Sources*, 2001, **102**, 270-276.

51   A. Hasbach, U. Retter, K. Siegler and W. Kautek, *J. Electroanal. Chem.*, 2004, **561**, 29-35.

52   F. La Mantia, J. Vetter and P. Novak, *Electrochim. Acta*, 2008, **53**, 4109-4121.

53   U. Troltzsch and O. Kanoun, *Electrochim. Acta*, 2012, **75**, 347-356.

54   M. T. McDowell, S. W. Lee, J. T. Harris, B. A. Korgel, C. Wang, W. D. Nix and Y. Cui, *Nano Lett.*, 2013, **13**, 758-764.

55   M. Gu, Y. Li, X. Li, S. Hu, X. Zhang, W. Xu, S. Thevuthasan, D. R. Baer, J.-G. Zhang, J. Liu and C. Wang, *ACS Nano*, 2012, **6**, 8439-8447.

56   M. Schmidt, U. Heider, A. Kuehner, R. Oesten, M. Jungnitz, N. Ignatev and P. Sartori, *J. Power Sources*, 2001, **97-98**, 557.

57   L. Ole Valoen, J. Reimers, *data obtained from E-one Moli Energy* (Canada).

58   S. Franger, F. Le Cras, C. Bourbon and H. Rouault, *J. Electrochem. Soc.*, 2002, **5**, A231-A233.

59   S. D. Beattie, D. Larcher, M. Morcrette, B. Simon and J.-M. Tarascon, *J. Electrochem. Soc.*, 2008, **155**, A158-A163.

60   Z.-J. Han, N. Yabuuchi, K. Shimomura, M. Murase, H. Yui and S. Komaba, *Energy Environ. Sci.*, 2012, **5**, 9014-9020.

61   Y. Liu, X. Qiu and X. Guo, *J. Mater. Chem. A*, 2013, **1**, 14075-14079.

254x63mm (150 x 150 DPI)